Persistence and Robustness of Lagrangian Coherent Structures

Mateusz Matuszak[1], Johannes Röhrs[1], Pål Erik Isachsen[12], and Martina Idžanović[1]

[1]Norwegian Meteorological Institute, Henrik Mohns Plass 1, 0371 Oslo, Norway

[2]Department of Geosciences, University of Oslo, P.O. Box 1022, Blindern, 0315 Oslo, Norway

Correspondence: Mateusz Matuszak (mateuszm@met.no)

Abstract. Lagrangian coherent structures (LCS) are transient features in ocean circulation that describe particle transport, revealing information about transport barriers and accumulation or dispersion regions. Various methods exist to infer LCS from surface current fields provided by ocean circulation models. Generally, Lagrangian trajectories as well as LCS analysis inherit the uncertainty from the underlying ocean model, bearing substantial uncertainties as a result of chaotic and turbulent flow fields. In addition, velocity fields and resulting LCS evolve rapidly. In this study, finite time Lyapunov exponents (FTLE) are used to detect LCSs in surface current predictions from a regional ocean forecast system. We investigate the uncertainty of LCS at any given time using an ensemble prediction system (EPS) to propagate velocity field uncertainty into the LCS analysis. We evaluate variability of FTLE fields in time and across the ensemble at fixed times. Averaging over ensemble members can reveal robust FTLE ridges, i.e. FTLE ridges that exist across ensemble realisations. Time averages reveal persistent FTLE ridges, i.e. FTLE ridges that occur over extended periods of time. We find that LCS are generally more robust than persistent. Large scale FTLE ridges are more robust and persistent than small scale FTLE ridges. Averaging of FTLE field is effective at removing chaotic, short-lived and unpredictable structures and may provide the means to employ LCS analysis in forecasting applications that require to separate uncertain from certain flow features.

1 Introduction

Oceanic flows transport various tracers, such as nutrients, plankton, and pollution. The dynamic processes that govern such transport span over several orders of magnitude (Röhrs et al., 2021), and the exact prediction of tracer fate is unfeasible due to the nonlinear chaotic nature of geophysical flow. Low predictability of ocean currents and the associated error propagation into trajectory calculations causes large uncertainties in any tracer transport study and forecast (e.g. Dagestad and Röhrs, 2019).

Velocity fields required for ocean transport studies are commonly obtained from Oceanic General Circulation Models (OGCMs). Velocity fields are highly sensitive to small variations in initial conditions, leading to uncertainties in a) the flow field and b) the resulting particle trajectories. This is reflected in numerical analyses, e.g. Lagrangian particle trajectories, which may yield large errors over time due to small errors in initial flow fields, position or time of release.

Lagrangian Coherent Structures (LCS) provide a diagnostic description of particle transport in complex dynamical flows independent of individual trajectories. Proposed by Haller and Yuan (2000), LCSs identify time-evolving shapes in unsteady and chaotic flow fields like eddies or jets, which influence trajectory patterns. Hyperbolic LCSs characterize attraction and

repulsion in the flow, whereas parabolic and elliptic LCSs describe trajectories in jets and vortex boundaries (Haller, 2015). In two-dimensional (2D) flows, hyperbolic LCSs manifest as one-dimensional (1D) curves, locally acting as the most attracting or repelling structures over a time interval. A key trait of hyperbolic LCSs is their role as effective transport barriers; material converges towards or diverges away from the LCSs without passing through them (e.g., Haller and Yuan, 2000; Lekien et al.,

30   2005; Dong et al., 2021). LCSs yield information about the flow field itself, in particular how the flow field organizes particles and where these are likely to be located. An application of LCS analysis in emergency response, e.g. oil-spill clean-up operations, has since been discussed (e.g. Olascoaga and Haller, 2012; Peacock and Haller, 2013).

Previous studies often discuss the LCS methodology and their practical applications, but rarely touch upon the topic of LCS estimates being inherently affected by uncertainties in the velocity fields they aim to describe. Furthermore, short-lived flow

35   features constantly develop, drift, and dissipate in real oceanic flow (Chen and Han, 2019). Given their time-dependency, LCSs might appear and disappear just as quickly. This brings up two important questions: (1) Given the velocity field uncertainty, how *robust*, i.e. predictable, are LCSs derived from ocean models at a particular time?; (2) Given their time-dependency, how *persistent* are LCS in ephemeral flows?

Dong et al. (2021) investigated the persistence of a transport barrier, detected as an LCS in the Lofoten-Vesterålen (LoVe)

40   region. The authors identify that the barrier emerges each April for the years considered (2010-2019) and persists for 49 days on average. A low resolution satellite altimetry product was used, which does not capture small-scale or short-lived structures. Nevertheless, the considered LCS was persistent for a limited time. In another recent study, Badza et al. (2023) investigate the effect of flow-field uncertainty on LCS computations in the Gul Stream, showing that different LCS detection methods respond differently to flow-field uncertainty, arguing a non-robust method is not reliable. However, the authors do not go into detail as

45   to which underlying dynamics cause robustness in LCSs.

Here, we elaborate on the idea that LCS analysis could reveal flow-field structures in the presence of uncertainty in the used ocean model. Uncertainty in circulation forecasts are typically quantified by running ensemble simulations with perturbed initial and/or forcing conditions, e.g. using an ensemble prediction system (EPS). The aim is that the ensemble spread of circulation realisations represents the ocean state uncertainty (e.g. Sakov et al., 2012; Idžanović et al., 2023). Ensemble

50   members differ by e.g. perturbed initial and boundary conditions, parametrizations, and are initiated based on a probabilistic spread which should be consistent with the model's uncertainty (Leutbecher and Palmer, 2007). Subsequently, an ensemble of trajectory simulations can be based on an OGCM ensemble, such that the spread of trajectories is based on the uncertainty in the flow field (de Aguiar et al., 2023).

Our study investigates the persistence and robustness of LCSs based on a high-resolution ocean EPS in the dynamically

55   active Lofoten-Veseterålen shelf sea region off Northern Norway. In section 2, we describe the used data set from an operational ocean forecast system and provide an outline of how the LCS analysis is performed using Finite-Time Lyapunov Exponents (FTLE). In section, 3 we present results invoking time-averages and ensemble averages of FTLE fields, respectively. In section 4, we draw conclusions on temporal and seasonal variability of LCS and uncertainties in the LCS analysis. Finally, we discuss implications on the applicability of the LCS analysis in uncertain flow fields as a tool in operational forecasting.

2 Data and methods

60

2.1 Study region
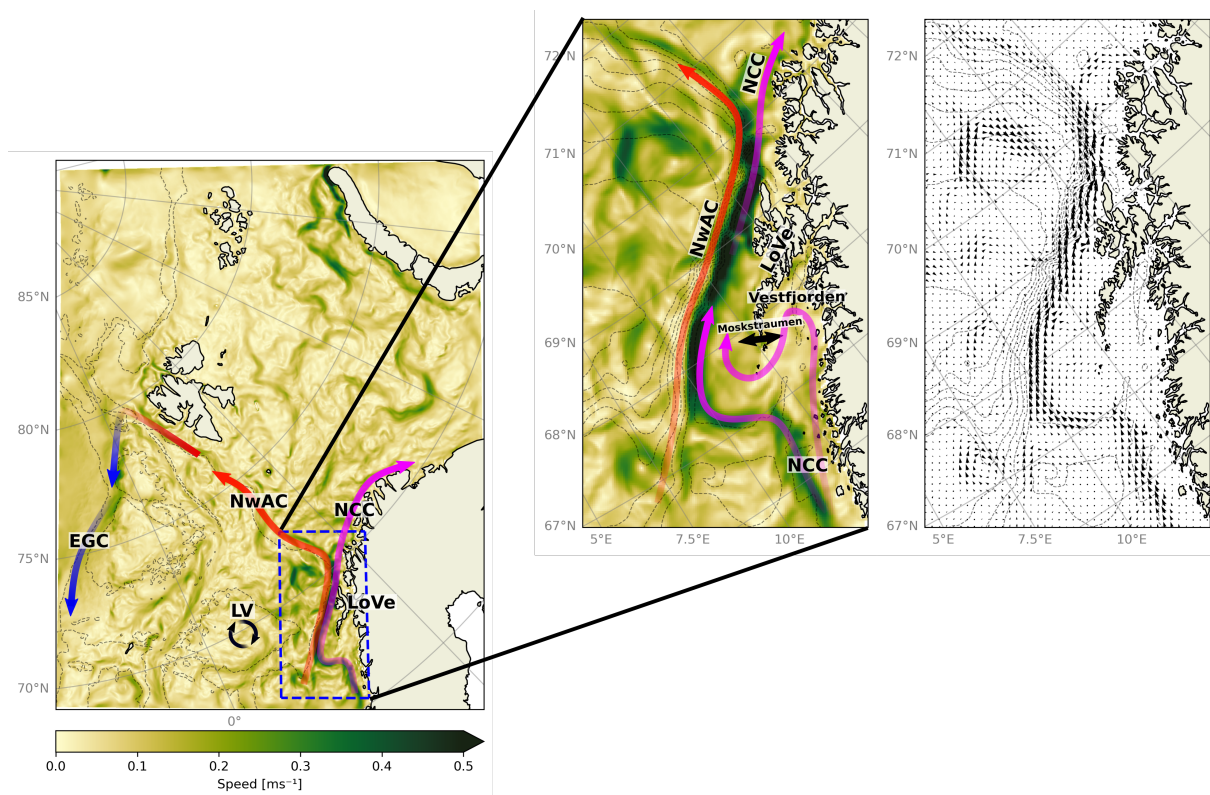
Figure 1. Average ocean current speed $[ms^{-1}]$ for the period 2023-02-01 to 2023-02-28 over the full Barents-2.5 model domain. Dashed blue lines highlight the region of interest for this study, which is the oceanic part around the Lofoten-Vesterålen islands (LoVe) and is enlarged. Arrows in the rightmost panel indicate average current velocities for the period. Bathymetry is indicated by gray dashed lines. Purple arrows indicate the Norwegian Coastal Current (NCC). Red arrows indicate the Norwegian Atlantic Current (NwAC). Blue arrows indicate the East Greenland Current (EGC). The circular black arrows indicate the Lofoten Vortex (LV). The two-headed black arrow indicates Mokstraumen.

The LoVe archipelago along northern Norway's coast in Fig. 1 is chosen for this study due to its ecological significance. Complex bottom topography and a steep continental slope steer the region's primary surface currents (Sundby, 1984); the Norwegian Atlantic Slope Current (NwASC) (Rossby et al., 2009) and the Norwegian Coastal Current (NCC) (Gascard et al., 2004). The fractal coastline and Vestfjorden have large implications on the NCC, causing complex flow features. During winter, southerly winds cause water mass accumulation along the coast and the geostrophic adjustment to the sea surface tilt can lead to increased current velocities (Mitchelson-Jacob and Sundby, 2001).

This particular region where NwASC and NCC converge is a hotspot for intense eddy formation and heat exchange along the Norwegian coast. An unstable front frequently forms between these currents at the steepest continental slope section, caused

70 by lateral and vertical current shear and the steep slope (Koszalka et al., 2013; Isachsen, 2015; Trodahl and Isachsen, 2018). Eddies formed in NwASC tend to break off and drift westwards, merging with the Lofoten Vortex (Søiland and Rossby, 2013).

2.2 Regional Ocean Ensemble Prediction System

As an example for ocean circulation in a coastal area with temporal varying flow, we use data from Barents-2.5 EPS (Röhrs et al., 2023), a coupled numerical ocean and sea-ice model based on the regional ocean modeling system (ROMS) (Shchepetkin

75 and McWilliams, 2005). The model has a 2.5 km horizontal and hourly temporal resolution, covering the Barents Sea, the coast off northern Norway and Svalbard (see Fig. 1). The system consists of 24 members, divided into four sets of six members. The sets are initiated with a 6-hour delay, at 00 UTC, 06 UTC, 12 UTC, and 18 UTC, with a forecast period of 66 hours. Each member is initialized by its own state from the previous day in order to preserve sufficient spread in the ensemble. The EPS forecast is initialized with largely varying initial conditions in the mesoscale circulation, as to represent model uncertainties.

80 The ensemble spread is further controlled by the Ensemble Kalman Filter data assimilation scheme, which reduces the spread of observed variables (Evensen, 1994; Röhrs et al., 2023). The first member in each set (four members) is forced by most recent atmospheric conditions from the AROME-Arctic model (Müller et al., 2017). The remaining members are forced by 20 members from the integrated forecast system developed by the European Centre for Medium Range Weather Forecasts (ECWF-ENS) (Röhrs et al., 2023).

85 ## 2.3 Lagrangian Coherent Structures

Various methods have been proposed for LCS detection in 2D flows, among which the FTLE is the most widely used (van Sebille et al., 2018). The distance between two neighbouring particles is assumed to grow exponentially over time in a chaotic system. Therefore, the distance δ_t between two particles at time t can be approximated as a function of the initial distance δ_0:

$$\delta_t \approx \delta_0 e^{\sigma t}, \tag{1}$$

90 where σ is the Lyapunov exponent, i.e. the separation rate (Rosenstein et al., 1993). FTLE finds the *maximum* separation rate between infinitesimal fluid parcels *over a finite time-interval* (Pierrehumbert and Yang, 1993). Because FTLE measures separation, i.e. repulsion, Haller (2001) and Shadden et al. (2005) argue that FTLE can identify *repelling* hyperbolic LCSs.

The LCS theory originates from the Lagrangian viewpoint, aiming to examine fluid transport based on Lagrangian principles. The FTLE method calculates the separation rate among fluid elements at fixed model grid points. Consequently, despite its

95 Lagrangian roots, the FTLE information is on an Eulerian grid.

FTLE's are calculated from flow fields provided by an OGCM following the method described by Haller (2001); Shadden et al. (2005); Farazmand and Haller (2012). The 2D movement of fluid parcels from their initial positions $\boldsymbol{x}_0$ at time t_0 to their final positions at time t is described by a flow map $\boldsymbol{F}_{t_0}^t(\boldsymbol{x}_0)$. As multiple fluid parcels are transported by the flow, the distance between neighbouring fluid parcels is likely to contract or expand over the time interval. At each point in space, the change in

separation between fluid parcels can be described by the Jacobian of $\boldsymbol{F}_{t_0}^t(\boldsymbol{x}_0)$:

$$\boldsymbol{\nabla} \boldsymbol{F}_{t_0}^t(\boldsymbol{x}_0) = \begin{bmatrix} \frac{\partial x}{\partial x_0} & \frac{\partial x}{\partial y_0} \\ \frac{\partial y}{\partial x_0} & \frac{\partial y}{\partial y_0} \end{bmatrix}, \tag{2}$$

where $\partial x_0, \partial y_0, \partial x$, and ∂y are the initial and final distances between particles in x and y directions. ∂x and ∂y are obtained by advecting fluid parcels:

$$\partial \boldsymbol{x} = \int \boldsymbol{u} \delta t, \tag{3}$$

where $\boldsymbol{x} = (x, y)$ is the parcels' position and $\boldsymbol{u} = (u, v)$ is the velocity field. This advection is calculated by OpenDrift (Dagestad et al., 2018), an open-source Python based software for Lagrangian particle modelling developed at the Norwegian Meteorological Institute. Eq. 2 is used to define the Cauchy-Green strain tensor $\boldsymbol{C}_{t_0}^t(\boldsymbol{x}_0)$ (Truesdell and Noll, 2004), which describes the speed and direction of deformation in the system

$$\boldsymbol{C}_{t_0}^t(\boldsymbol{x}_0) = \left[\boldsymbol{\nabla} \boldsymbol{F}_{t_0}^t(\boldsymbol{x}_0)\right]^* \boldsymbol{\nabla} \boldsymbol{F}_{t_0}^t(\boldsymbol{x}_0). \tag{4}$$

It can then be shown that the FTLE field is given by

$$\sigma_{t_0}^t(\boldsymbol{x}) = \frac{1}{|T|} \ln \sqrt{\lambda_{max}\left(\boldsymbol{C}_{t_0}^t\right)}, \tag{5}$$

where T is the time interval, chosen as 24 hours for our simulations, over which the FTLE is computed and $\lambda_{max}\left(\boldsymbol{C}_{t_0}^t\right)$ is the largest eigenvalue of $\boldsymbol{C}_{t_0}^t(\boldsymbol{x}_0)$ corresponding to the dominant stretching in the system. It can be shown that repulsion in a system is attraction in the same system over a reversed time-frame. Thus, a repelling LCS over the backwards time interval is an attracting LCS over the forwards time interval. The absolute value of T allows for integration both forwards and backwards in time. Finding the largest FTLE (largest stretching) forward-in-time will result in detection of repelling LCSs, whereas the largest FTLE backward-in-time yield attracting LCSs forward-in-time (Haller, 2001; Shadden et al., 2005; Farazmand and Haller, 2012). Attracting LCSs are interesting from an ecological standpoint, as these can e.g. describe nutrient or pollution accumulation regions. We will therefore focus on attracting LCSs, although LCS robustness and persistence should apply for both.

FTLE averages over ensemble members and time are calculated to identify robust and persistent features. Variations among members and over time are expected due to perturbed velocity fields and time dependency. Averaging might unveil similarities across both members and time. The notations $\overline{F}_m$ and $\overline{F}_t$ denote the ensemble and time averages, respectively. The standard deviation gives a measure of the spread in the sample distribution, and is denoted as σ_m and σ_t for the ensemble and time standard deviations, respectively.

LCSs, which are infinitesimally thin 1D curves in 2D flow fields are approximated by FTLEs with 2D curves with a finite width. A conceptual example of FTLE ridges and their average is shown in Fig. 2. The ridges act as repellors or attractors at distinct locations. Averaging smooths the ridges into a field of repulsion/attraction, ultimately indicating a region where FTLE ridges are statistically likely to form. On the other hand, if the individual FTLE ridges would be more similar to each other, linear features should still be present in the average, making these ridges more certain and/or persistent.

The ensemble average, $\overline{F}_m$, and the time average, $\overline{F}_t$, should not be considered as definitive transport barriers. It is unclear whether LCSs constituting these averages originate from the same model realization or exist simultaneously. It is also uncertain whether an average consists of a few long LCSs or many short ones. The former act as transport barriers over larger regions, while the latter permit material drift between them. Instead, we consider $\overline{F}_m$ and $\overline{F}_t$ as average accumulation or dispersion regions, *potentially* containing transport barriers.
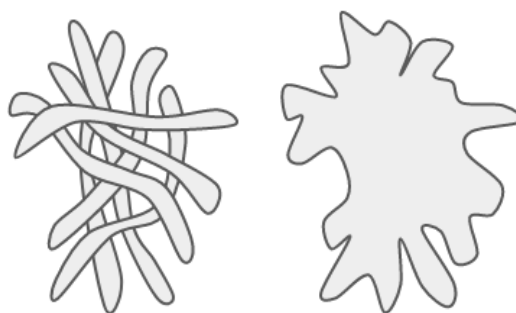
Figure 2. Schematic representation of individual FTLE ridges (left) and the average region covered by them (right).

3 Results

Firstly, we present the temporal evolution of the FTLE and detect persistent FTLEs through the time average. Secondly, FTLEs from individual EPS members and their average are presented to highlight uncertainties in the FTLE field given an uncertain velocity field to detect robust features. Finally, spatial and spectral analysis of the FTLE fields are presented to provide a more comprehensive analysis of FTLE robustness and persistence.

3.1 Persistence of Lagrangian Coherent Structures
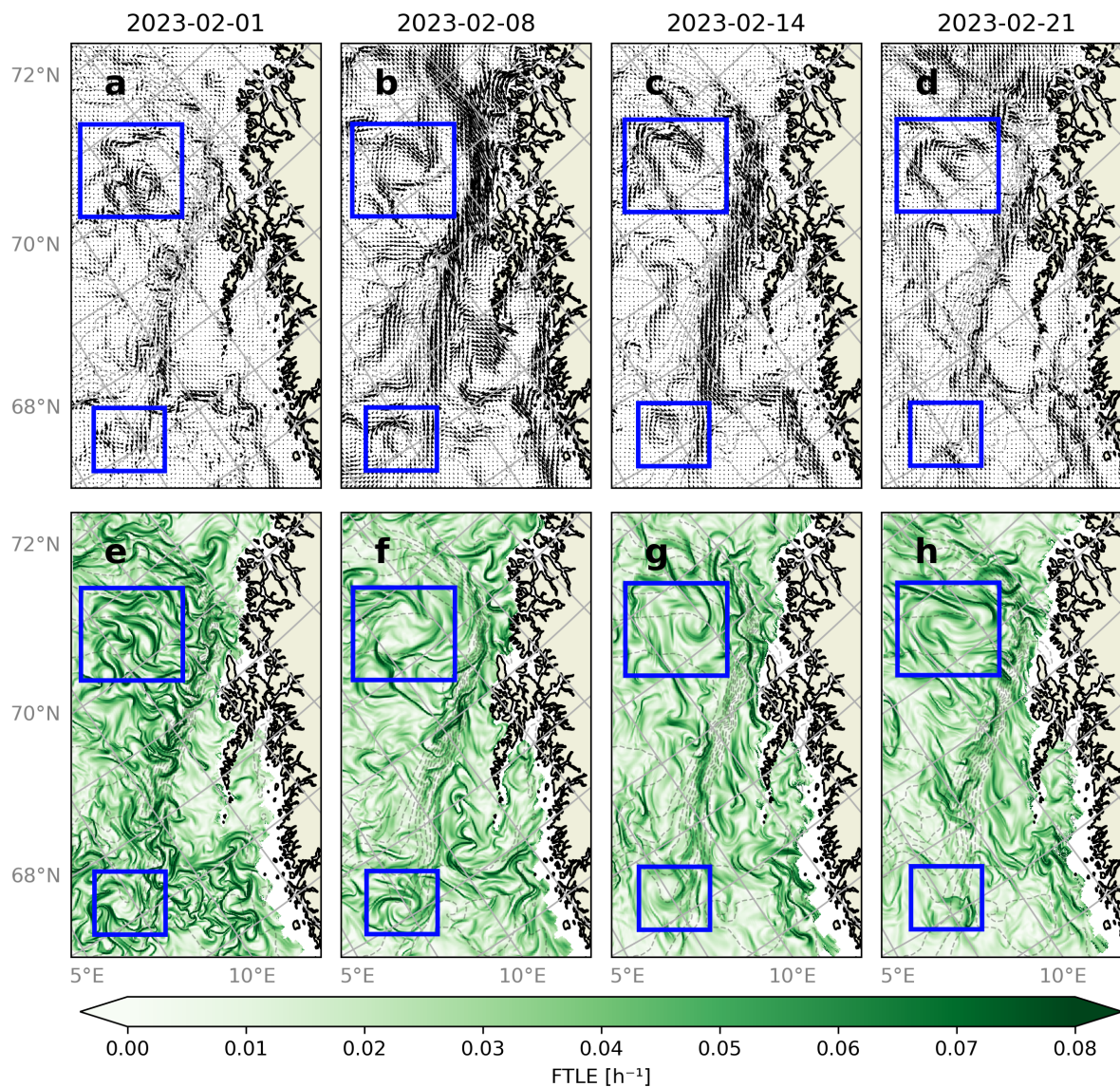
Figure 3. Instantaneous surface velocity fields (top row) and corresponding FTLE ridges that approximate attracting LCSs (bottom row) during four selected dates: a,e) 2023-02-01, b,f) 2023-02-08, c,g) 2023-02-14, and d,h) 2023-02-21 at time 00:00. The bathymetry is indicated by gray dashed lines. Two persistent eddies are highlighted with blue boxes.

Velocity fields and corresponding backwards FTLEs from first AROME-Arctic-driven member (henceforth called the reference member) of the Barents-2.5 EPS are shown in Fig. 3 for four exemplary dates one week apart in February 2023. Note that FTLE

ridges approximate LCSs. Additional criteria for a distinction of LCS from FTLE fields are given by Farazmand and Haller

145 (2012) but are not evaluated here. Hence, we evaluate the variability of FTLE fields.

The intensity and meandering of the coastal current, as well as details in the eddy field change from week to week in Figs. 3a-d. However, the two highlighted eddies are present in the three first weeks. These are considered to be persistent flow features over the time period.

The FTLE field changes in Figs. 3e-h along with the velocity field. In general, no FTLE ridges stay the same between the

150 time steps, even in regions where the flow itself appears largely persistent, e.g. the two highlighted eddies. Thus, the associated LCS are highly ephemeral, changing rapidly with the flow.

We note that there are more FTLE ridges in the domain in the first time step, indicating that velocity gradients cause material accumulation. This can e.g. be seen in the eddies in the region, which are often represented by circular linear features in the FTLE field. The current strength itself has little effect on material accumulation, as seen in the two middle time steps of Fig. 3,

155 where the current is strong along the continental slope but the region does not exhibit particularly many FTLE ridges.

We know that even though the flow field is changing, some flow features will always exist on average over time. In the case of the LoVe region, strong currents along the continental slope (NwAC and NCC) are present on average. Similarly, FTLEs vary in time, but certain regions frequently exhibit FTLE ridges. The FTLE time average, $\overline{F}_t$, will reveal these regions.
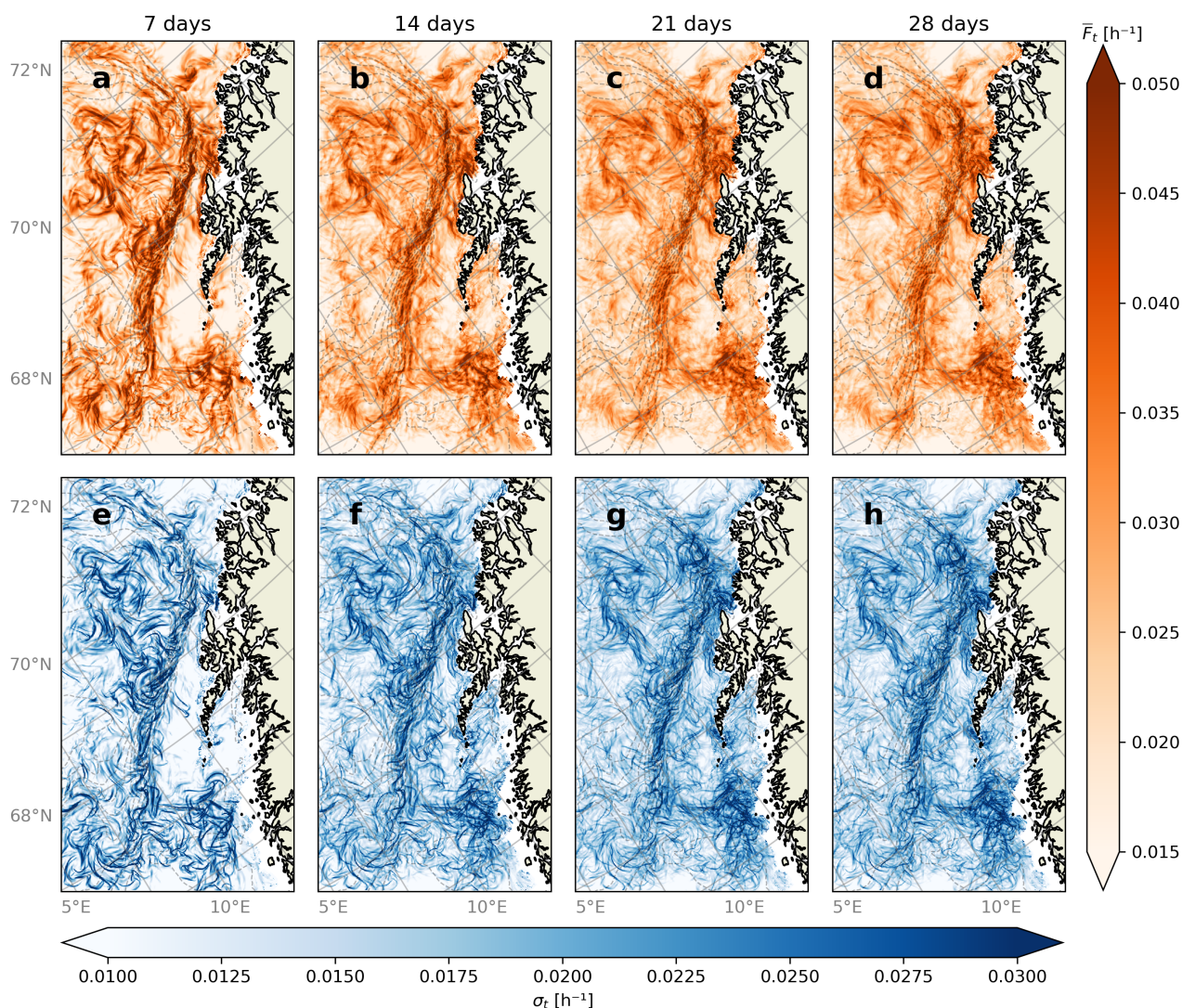
Figure 4. FTLE time averages, $\overline{F}_t$, (orange) and standard deviation over time, σ_t (blue) around the LoVe region for four different time periods starting on 2023-02-01: a,e) 7 days, b,f) 14 days, c,g) 21 days and d,h) 28 days. The FTLE analysis is based on velocities from a single ensemble member (reference member) of the Barents-2.5 EPS. Dashed gray lines indicate bathymetry.

FTLE averages and standard deviations over time, $\overline{F}_t$ and σ_t, are shown in Fig. 4 for different averaging lengths. Longer averaging periods effectively reduce variability in $\overline{F}_t$. Strong linear features in $\overline{F}_t$ can be distinguished for shorter averaging times in the domain, indicating a degree of short term persistence. However, these features become more diffused in $\overline{F}_t$ with higher averaging periods, and individual FTLE ridges disappear for averaging times of 30 days or longer.

Even though FTLE ridges are seen to be ephemeral in Fig. 3, high valued $\overline{F}_t$ regions indicate where FTLE ridges are frequently situated over time. Most notably, $\overline{F}_t$ indicates frequent FTLE ridges along the continental slope during February

165 2023, where the mean flow is most significant. FTLE ridges are less frequent on the continental shelf and over the deep ocean. Both notions are independent of averaging time. Furthermore, the two eddies indicated in Fig. 3 are persistent in the mean flow in Fig. 1, and frequent FTLE activity is present in the same regions. This result indicates that, unsurprisingly, FTLE ridges are persistent where the current itself is persistent.

The large variability over time is further emphasized by the standard deviation σ_t. Regions with high $\overline{F}_t$ are usually accom-
170 panied by high σ_t, affirming a positional and structural evolution. Note that σ_t will be large with small positional perturbations of FTLE ridges.

3.2 Seasonal variations
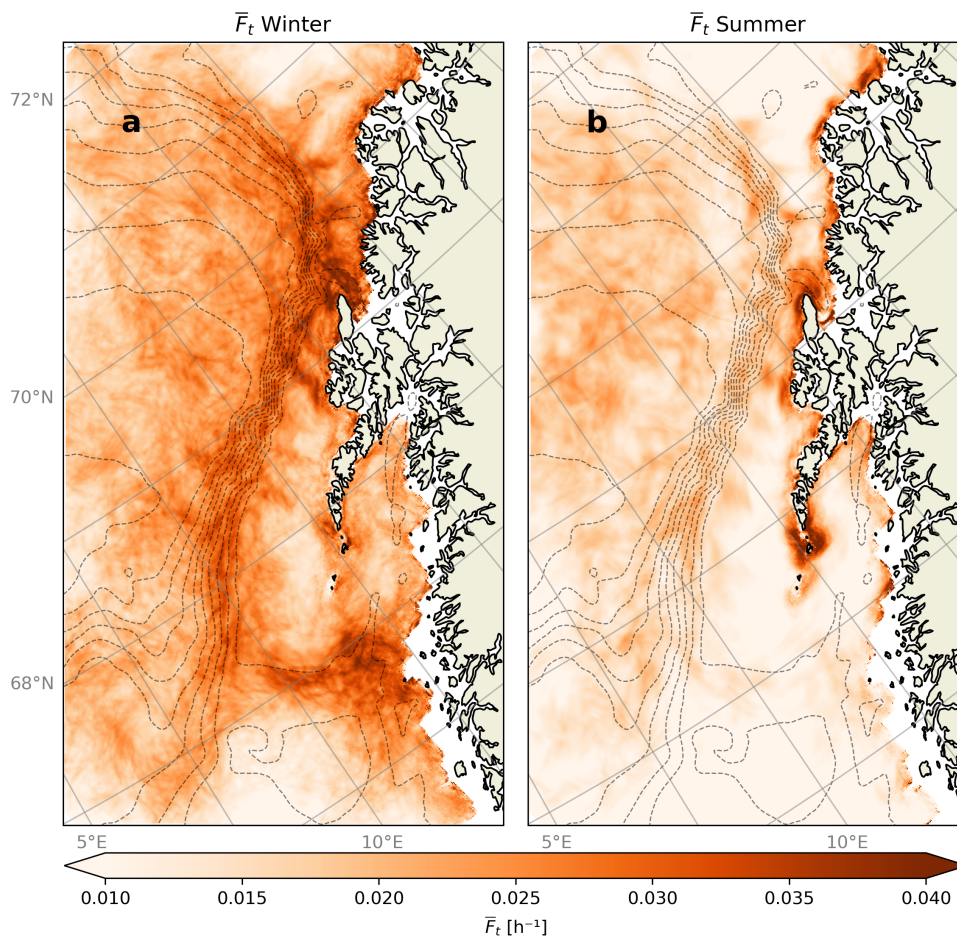
Figure 5. Seasonal FTLE averages for a) winter and b) summer. Months included in the winter season are December 2022, January 2023, and February 2023. Months included in summer season are June 2023, July 2023, and August 2023. Dashed gray lines indicate bathymetry.

Seasonal averages, $\overline{F}_t$, for the winter and summer seasons are shown in Fig. 5. FTLEs indicate a frequently occurring transport barrier along the continental slope during winter, but not during the summer season. Both seasons exhibit large activity near the northern tip of LoVe, with the summer season showing higher activity around Mokstraumen.

The high $\overline{F}_m$ around Mokstraumen is directly connected to formation of strong jets at the strait exit. The direction of the current through the strait is dependent on the tidal phase (Børve et al., 2021). After closer investigation, FTLE ridges tend to form only on one side of Mokstraumen at any particular time, depending on current direction and thus the tidal phase. Therefore, a predictable tidal dependent periodic variability of FTLEs exists here. An indication of this phenomena is seen to a lesser extent during winter.

3.3 Robustness of Lagrangian Coherent Structures
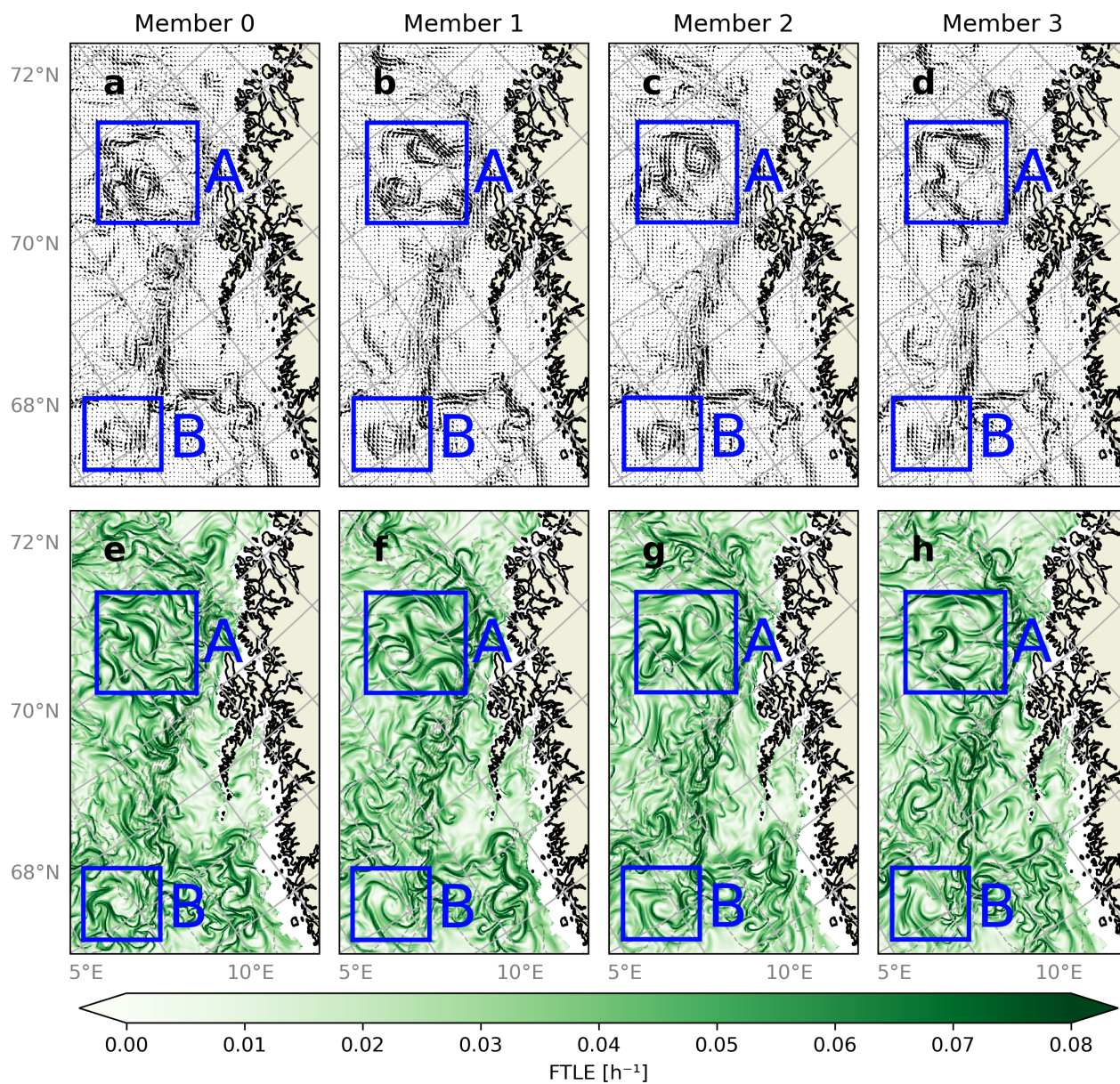
Figure 6. a,b,c,d) Velocity fields from four different Barents-2.5 EPS ensemble members at the LoVe region at 2023-02-01 and e,f,g,h) corresponding backward FTLEs. Two regions of interest are highlighted with blue boxes.

We investigate the robustness of FTLE predictions, i.e. whether FTLE ridges predicted by an OGCMs are similarly present in an ensemble of flow realisations. Velocity fields and FTLEs of four randomly selected members are shown in Fig. 6. Generally,

the displayed set of FTLE fields show that FTLE ridges appear in similar regions, but their position is shifted and linear features
have different lengths and shapes. Nevertheless, we identify particular FTLE ridges that exist across ensemble members, with
slight variations.

Two regions containing eddies in the flow field are highlighted with boxes in Fig. 6. The eddies in the highlighted regions
are generally represented by circular FTLE ridges. A clearly defined eddy is found in box A in all members, with member 1
containing two eddies. The bottom eddy in member 1 has a similar position to the eddy in member 0, whereas the top eddy
in member 1 has a similar position to the eddies in members 2 and 3. The eddies in box A in members 1-3 are represented by
clearly defined circular FTLE ridges. Ignoring the bottom eddy in member 1, these circular FTLEs center around approximately
the same point, although the shape and sizes of the circles vary. However, it is hard to discern the eddy in member 0 in the
FTLE field, even though it appears to be similar to the bottom eddy in member 1. Box B highlights another eddy which is
similar between members, both in position and size. The FTLE representation appears similar, although the circle in member
0 appears rougher than in the rest.

On closer inspection, all members of the Barents-2.5 EPS predict eddies in the box A region, some of which predict one eddy
in a similar position to members 2 and 3 in Fig. 6, whereas others predict two or more eddies, similarly to member 1. However,
some members represent the eddies with circular FTLE ridges, whereas the circles are hard to discern in other members. A
similar analysis of the region in box 2 reveals that this eddy is present in most members, hence is considered to be certain.
Differences in FTLE ridges are more apparent than in the flow field, and similar flow features can have both similar or different
FTLE representations.
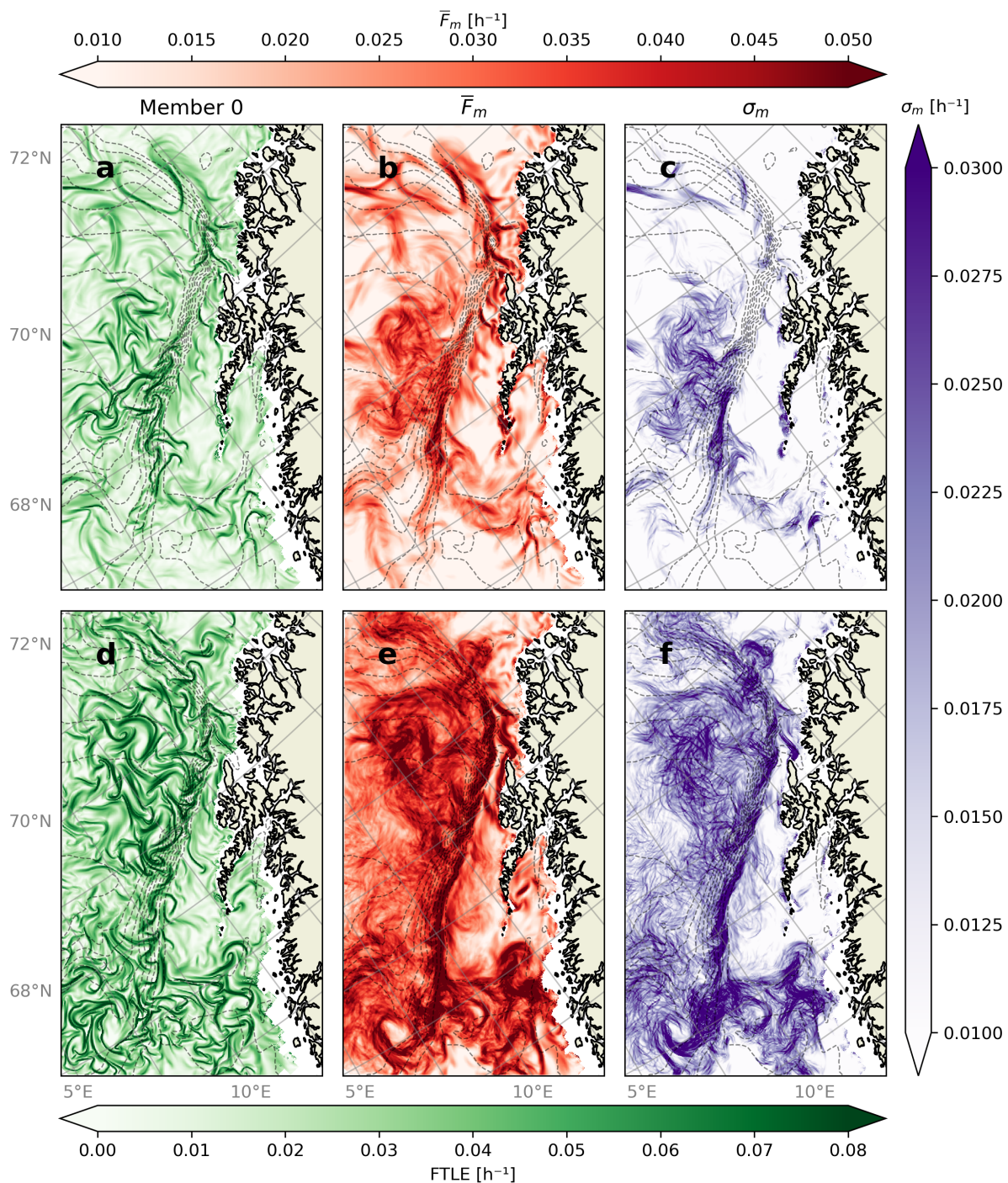
Figure 7. FTLE fields around the LoVe region at 2023-01-02 (top) and 2023-02-02 (bottom) computed using velocity fields from the Barents-2.5 EPS. a,d) FTLE fields (green) from member 0. b,e) averaged FTLE fields (red) over the ensemble. c,f) standard deviation of the FTLE fields (purple) over the ensemble. Bottom topography indicated with dashed gray lines.

Instead of inspecting the FTLEs of each member individually, the ensemble averaged FTLE field, $\overline{F}_m$, allows us to detect robust features; linear features will be present in $\overline{F}_m$ where individual members predict the FTLE ridges similarly. FTLE fields for the reference member, $\overline{F}_m$ and the ensemble standard deviation FTLE, σ_m, are shown for two dates in Fig. 7.

205 Both dates exhibit clearly distinguishable linear features in $\overline{F}_m$ along the continental slope, although these are stronger and longer on 2023-02-02. While these linear features in $\overline{F}_m$ are long, continuous and tangent to the continental slope, FTLE ridges in individual members are thinner, shorter and often not tangent to the continental slope. $\overline{F}_m$ shows where majority of members predict FTLE ridges, but not exactly how these look like. A large σ_m further emphasizes the structural and positional variability of individual FTLE ridges along the continental slope. Even so, because of the strong signal in $\overline{F}_m$, the FTLEs

210 along the continental slope are robust.

Two additional regions are identified and considered as robust in Fig. 7. These are the u-shaped structure in the north at 2023-01-02 and the circular shape in the south at 2023-02-02, which are enlarged in Fig. 8. The u-shaped structure exhibits thin, distinguishable features with little noise around them, and corresponding σ_m indicates small variability around $\overline{F}_m$, implying high agreement between members. Inspecting each member individually reveals this to be true, thus linear features in $\overline{F}_m$

215 represent individual members well. This u-shaped structure is therefore highly robust at this particular time.
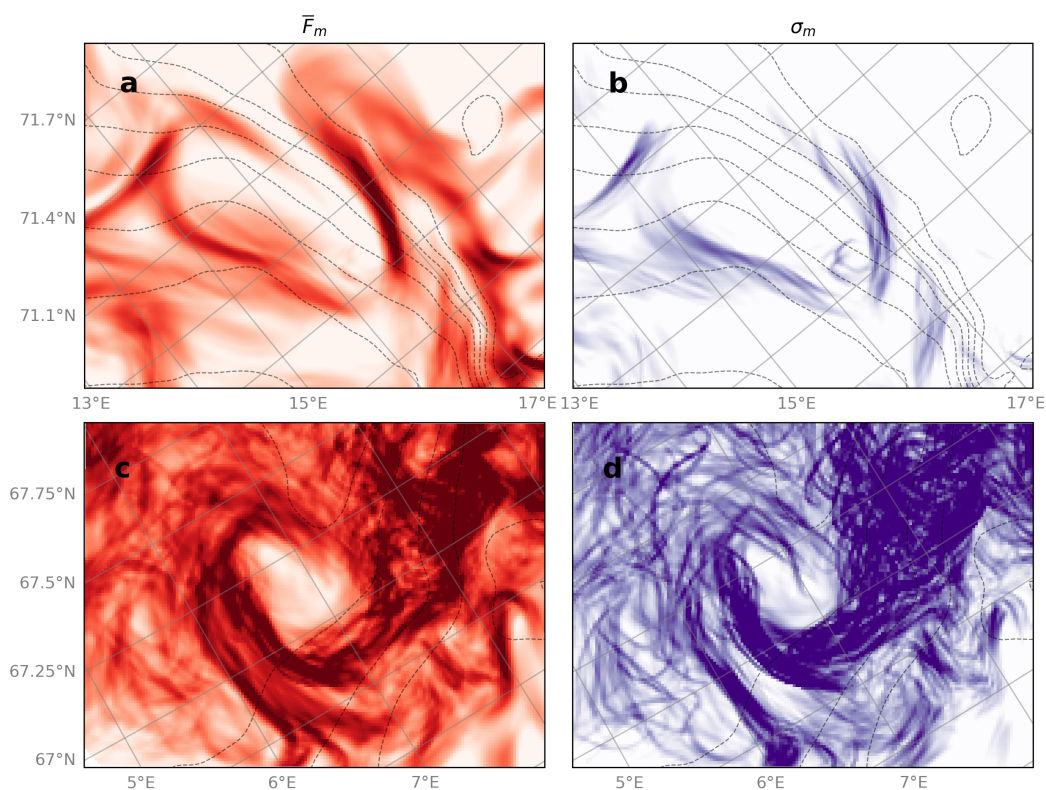
Figure 8. Detailed map of the two regions highlighted in Fig. 7. a) ensemble average for 2023-01-02, b) ensemble standard deviation for 2023-01-02, c) ensemble average for 2023-02-02, and d) ensemble standard deviation for 2023-02-02.

The circular linear features in $\overline{F}_m$ in Fig. 8 represent the same eddy as seen in Fig. 7 one day later. There is more noise around this feature than the u-shaped structure, but a circle can still be distinguished in $\overline{F}_m$. Individual members generally agree on this feature, but disagree on the FTLE field around said structure. The large σ_m reveals that members disagree on its exact shape and position. Therefore, this structure can be considered robust, although its exact appearance is more uncertain than the u-shaped structure.

Finally, there is a region to the left of the continental slope in Fig. 7b which exhibits high values in $\overline{F}_m$, but all linear features have been smoothed out. Combined with the high σ_m in this location, it can be concluded that there is a high probability of strong linear features existing in this region, but these are non-robust and their position and shape is indeterminable from $\overline{F}_m$. Therefore, an FTLE average can yield both distinguishable linear features in the domain, as well as large smooth fields. Linear features are associated with robustness, indicating higher certainty, whereas a smooth field yields regions where linear features are likely to be found. Often a high $\overline{F}_m$ is accompanied by a high σ_m, but this might simply be a result of small positional perturbations of the thin linear curves, and does not necessarily indicate significant variability. Therefore, the highlighted regions are considered to be robust for the particular dates.

3.4 Properties of ensemble and time averaged FTLE fields
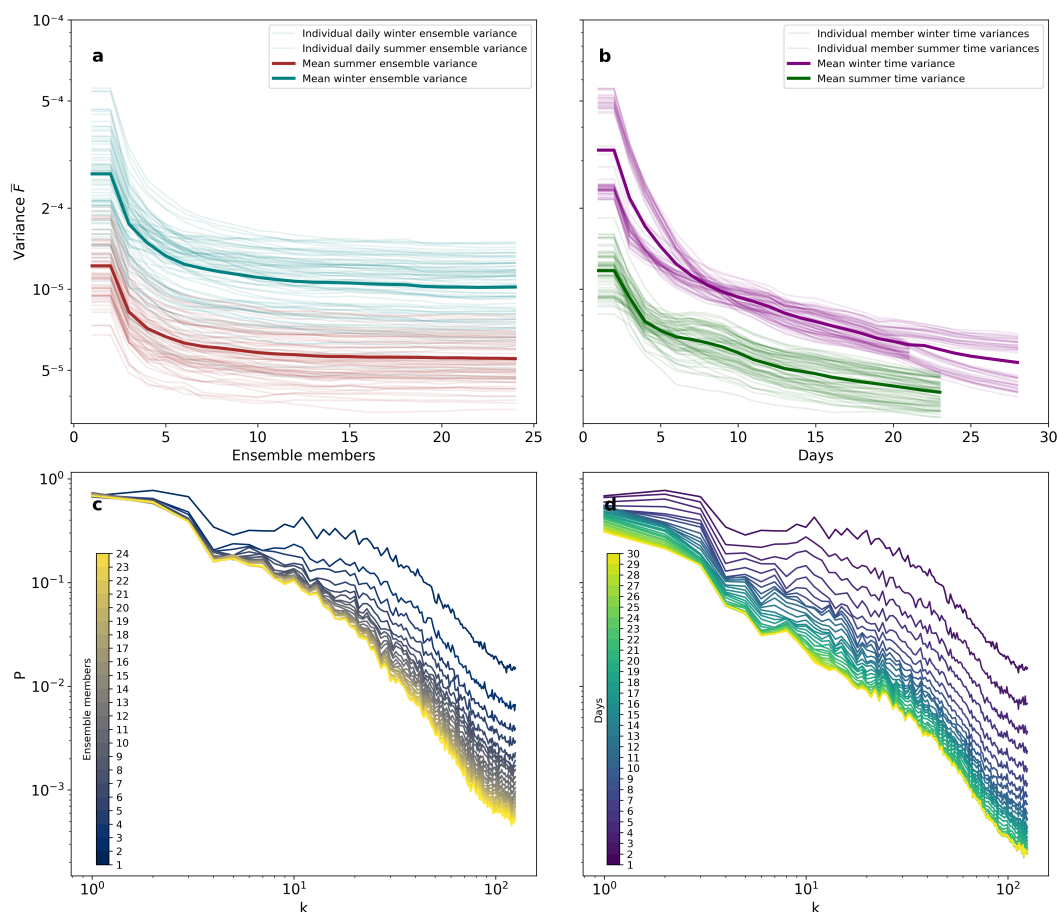
Figure 9. Spatial and spectral variance of FTLEs and averaged FTLEs. a) Spatial variance over the ensemble average. Thin blue and red graphs indicate individual days during the winter and summer seasons, and the thicker blue and red graphs are the average of the thin graphs. b) Spatial variance over the time average. Thin purple and green graphs indicate the evolution of variance during the winter and summer months as up to 30 days are considered in the time average for each member. c) Spectral distribution of spatial FTLE variance in ensemble averages as an increasing number of members are considered in the average, averaged over all days in winter. d) Spectral distribution of spatial FTLE variance for time averages as an increasing number of days are considered in the average, starting from 2023-01-01, averaged over all members. Colorbars in c) and d) indicate how many members or days the FTLE fields are averaged over.

230   Robustness and persistence of FTLEs are compared by their spatial and spectral variance, shown in Fig. 9. The spatial variance has been computed by averaging FTLEs over an increasing number of members or days, then computing the variance over the resulting averaged FTLE field. For the spectral variance, three 200km×200km non-overlapping sections without land have been selected. Each section is transformed into Fourier-space, and the power spectrum is computed for each grid row and

column. Resulting power spectrum over all rows and columns over all sections are then averaged to produce the final spectral
variance shown in Fig. 9. Similarly to the spatial variance, the FTLE fields are first averaged over an increasing number of
members or days before conducting this computation of the spectral variance.

The spatial variance ascertains that the degree of smoothing increases as more members or time steps are considered in the
FTLE averages. The smoothing rate of FTLE fields is independent of season, although the variance is lower during summer
due to lower FTLE activity as seen in Fig. 5. This smoothing factor is strong and similar for both averages for the first $\sim$5
members and time steps. The strong decay in the beginning of the $\overline{F}_m$ variance implies that there is a sufficient spread in the
ensemble, although $\overline{F}_m$ is dependent on which members are included in the average for few members. The spatial variance of
$\overline{F}_m$ stabilizes once $\sim$10 members are considered, implying the existence of distinct non-chaotic and highly predictable flow
features in the ensemble. Meanwhile, the spatial variance of $\overline{F}_t$ continues diminishing, signifying that FTLE ridges are more
robust over many members than persistent over long time periods.

The spectral variance shows how energy is distributed across wavenumbers. Energy diminishes as more members and time
steps and included in the averages, with the energy dissipation rate being largest for few members and time steps, coherent
with the smoothing factor in the spatial variance. Energy dissipates stronger for $\overline{F}_t$ than $\overline{F}_m$ at all wavenumbers, but is similar
at the largest wavenumbers, i.e. smallest scales. Small scale flows, thus also small scale FTLE ridges, are generally chaotic and
short-lived, thus are uncertain between members and evolve rapidly. Energy dissipates slowest at the largest scales, as large
scale flow features are generally less chaotic and more predictable and persistent. Minimal energy dissipation is seen at the
largest scales for $\overline{F}_m$, signifying that large scale structures are generally certain in the ensemble.

These results show that FTLE ridges are more robust than persistent at all scales. Energy dissipation happens fastest at
medium to small scales due to the chaotic and ephemeral nature of features at these scales. The strong decline at the beginning of
the spatial variances is due to small scale FTLE ridges experiencing a strong and quick smoothing, and slows down afterwards
as mostly large scale FTLE ridges are left. The spatial variance of $\overline{F}_m$ stabilizes because large scales features that are left in
the system do not dissipate. $\overline{F}_t$ continues being smoothed at all scales due to FTLE ridge formation, drift, deformation and
dissipation happening at all scales.

4   Discussion

Using ridges in FTLE fields as proxy, we see that LCS are variable across ensemble members and time. Potentially robust and
persistent structures have been identified by averaging out the transient and uncertain features. In this section the following
will be discussed: i) the persistence of FTLE ridges, ii) seasonality and iii) robustness.

4.1   Temporal variability of Lagrangian Coherent Structures

The flow field, and associated FTLE field, is seen to vary drastically over short time periods. Flow features that develop FTLE
ridges will drift, deform and dissipate over a range of time scales. The lifetime of a particular FTLE ridge is restricted by

265   the lifetime of the flow structure it represents. As a consequence, we expect that some LCS persist over time, particularly the structures formed by large scale circulation as these typically imply longer time scales.

In the LoVe region, FTLE ridges are seen to frequently form along the continental slope during winter. Particular FTLE ridges can be distinguished from $\overline{F}_t$ for short time averages, but the smoothing of the FTLE field increases with averaging time. The small scale FTLE ridges, being more chaotic and short lived, are smoothed at the highest rate, whereas the large
270   scale FTLE anomalies remain visible for longer averaging times. Thus large scale structures are more persistent and mainly these define where $\overline{F}_t$ indicate frequent LCS activity, especially for longer time averages.

Permanent geomorphological features present a defining constraint on the ocean circulation, e.g. large-scale bathymetry steers ocean currents at high latitudes (Gille et al., 2004). Frequent FTLE ridges along the continental slope in the LoVe region are formed by the persistent topography-steered NCC and NwAC. Dong et al. (2021) detected a persistent LCS transport
275   barrier along the continental slope at LoVe. Our results are based on a different time period, scale, and detection method, i.e. Dong et al. computed *repelling* LCSs using the Finite-Size Lyapunov Exponent method from altimetry, which generally do not coincide with the FTLE approach (Karrasch and Haller, 2013). Furthermore, our velocity fields are of higher spatio-temporal resolution, hence detecting smaller and more transient structures. Using time and ensemble average, however, we are able to find agreement with the structures detected by Dong et al. (2021). Appropriate time or ensemble averaging enables retrieval of
280   large scale transport barriers using high-resolution ocean models.

A weakness in time averaging of FTLE fields is that details in shape and direction of LCS are lost in $\overline{F}_t$. As discussed in Sec. 2.1, the average may consist of a few long, continues long-lived FTLE ridges, which result in continuous transport barriers, or many short and transient ridges allowing for material exchange. Other methods for detecting persistent LCS could yield more nuanced results, e.g. as used by Dong et al. (2021). The authors defined a set of criterion for the existence of a transport barrier
285   and investigated the frequency of the criterion being fulfilled. Another approach could be to select a particular FTLE ridge and study how it evolves over time. Its lifetime, propagation distance, growth/dissipation-rate and structural evolution could then be studies. Possibly, a relation between FTLE ridge size, strength and its lifetime could be established.

Time averaging of FTLE fields provides information about where FTLE ridges frequently form. Analysis of time averaged FTLE and LCS is useful for identifying regions of material accumulation and entrapment. For instance, the semi-permanent
290   anti-cyclonic eddy in the middle of the Lofoten Basin (Raj et al., 2015; Isachsen, 2015) forms persistent and re-occuring FTLE ridges Fig. 8. Furthermore, the canyons in the LoVe region host a multitude of aquatic organisms, e.g. cold water coral reefs, which is possible because of the nutrient accumulation here (Sundby et al., 2013; Bøe et al., 2016). We argue that these canyons will contribute to formation of persistent LCS, providing a control mechanism for particle transport towards specific locations.

4.2 Seasonal variability

295   Ocean currents in the LoVe region show seasonal variability in response to atmospheric forcing and seasonal hydrography. Autumn and winter months are characterized by westerly winds with transient low pressures passing the region, while spring and summer winds can be dominated by moderate easterly winds (Furnes and Sundby, 1981). During spring and summer,

seasonal stratification sets as response to freshwater runoff and solar radiation (Christensen et al., 2018). The associated ocean circulation patterns are reflected in the FTLE fields.

300   Pronounced LCS develop in different locations during the seasons; FTLE ridges occur along the continental slope during winter and closer to the coastline during summer. Seasonal stratification due to surface heating during summer leads to a decoupling of the ocean surface layer from deeper currents, thus bathymetry has a weaker impact on both robustness and persistence of surface flow structures during summer. A well-mixed water column during winter results in more barotropic flow, hence the bathymetry controls winter circulation and FTLE ridges develop in the lateral shear region along topography-

305   following slope currents. Note that FTLE ridges and transport barriers along the continental slope can still occur in summer, but seem to have a smaller impact on transport.

The coastline is expected to have a similar impact on FTLE formation throughout the year, as it directly affects surface currents. However, around Moskstraumen (Figs. 1 and 5) we identify higher FTLE variability in summer that is tied to tidal pumping through the narrow sound. Surface-intensified flow as a consequence of distinct summer stratification may amplify

310   surface currents in this particular location (Sperrevik et al., 2017).

The higher LCS activity during winter may be connected to more energetic flows at the 1-100km scale during this season. These flows are intensified by baroclinic instabilities formed around geostrophic eddies, and are much stronger during winter than summer (Callies et al., 2015).

4.3   Uncertainty of FTLEs in flow field

315   Ocean current uncertainty stems from non-linear equations of motion: small errors in initial conditions cause large errors in numerical integrations (Lorenz, 1963), and error propagation may cause large impact in trajectory simulations (e.g. Zimmerman, 1986; de Aguiar et al., 2023). By this argument uncertainty in LCS estimates derived from uncertain current fields is expected. In addition, uncertainty from the impact of wind drag on surface LCS must be expected for realistic drift applications (Allshouse et al., 2017). The Barents-2.5 EPS used in this study describes uncertainties of ocean currents in the analysis

320   and throughout the forecast range, with the notion that most extreme velocities are slightly underestimated (Idžanović et al., 2023). By calculating FTLE's for each ensemble member, we propagate the ocean model uncertainty into the LCS analysis presented here. We see that variability in FTLE ridges occur both positionally and structurally between members. FTLE ridges that exist in only one or few members are statistically unlikely to exists (compare Fig. 6), emphasizing the need of an EPS when employing LCS in operational oceanography.

325   Ensemble averaging is here suggested as a method to detect robust LCSs, i.e. FTLE ridges that appear in majority of members and can therefore be considered likely to exist, despite uncertainties in the underlying flow. Similarly to the time average, the ensemble average smooths out FTLE ridges resulting in regions where these are more likely to form. Some FTLE ridges can still be distinguished in $\overline{F}_m$, even after considering all 24 ensemble members of the Barents-2.5 EPS (Fig. 9). In particular, FTLE ridges situated along the continental slope tend to be more robust. The bathymetry plays an important role in forming

330   robust FTLEs, because even though the surface currents themselves are uncertain, the bathymetry constrains surface currents equally across the ensemble.

The spectral analysis (Fig. 9) showed that large scale FTLE features are more robust FTLEs, as variability does not decay at low wavenumbers when increasing number of ensemble members in the averaging. Smaller scale features are also present each individual member, but these are effectively removed by the ensemble average. Small scale flows are more chaotic and exhibits

335   lower predictability. In the LoVe region, large scale eddies exist in the majority of the Barents-2.5 EPS members. Individual FTLE ridges formed by these larger scale eddies are seen to vary between members, however, these can still be distinguished in the ensemble average $\overline{F}_m$. We conclude that FTLE ridges associated with larger scale flows are more robust than small scale FTLEs formed by more chaotic flows.

Sensitivity of the FTLE method has previously been investigated using satellite altimetry products by Harrison and Glatz-

340   maier (2012) and Badza et al. (2023). Both studies concluded that FTLEs are fairly insensitive to noise included in the velocity fields. Harrison and Glatzmaier (2012) finds that FTLEs are robust for large scale eddies and strong jets, whereas Badza et al. (2023) observes smoothing of the FTLE field due to ensemble averaging and consistency between FTLE fields across an ensemble. In addition, (Gouveia et al., 2020) argue that persistent large scale feature in particular give rise to quasi-steady LCS, such as the feature reported by (Dong et al., 2021) which is also analysed in our study. In addition to time-persistent features,

345   we investigate LCS detections from transient flow features. The Barents-2.5 EPS model used in this study can represent smaller and more transient structures than the aforementioned satellite products, and we can argue that FTLEs are more uncertain at smaller scales, but robust of the flow is constrained by coastal or bathymetric steering.

4.4   Implications for application of LCS analysis

Operational forecasting

350   Operational use of LCS analysis in forecasting, e.g. for search-and-rescue, oil-spill operations or path-planning (e.g. Beegle-Krause et al., 2011; Ramos et al., 2018; Serra et al., 2020), should be viewed together with the uncertainty ocean current predictions. LCSs can yield the much needed information about material accumulation regions and transport barriers, which could prove vital for saving lives or mitigate environmental catastrophes. Although FTLE ridges are variable across an ensemble, we see that some FTLE ridges are more robust than others. An ensemble of FTLE must be assessed to separate robust from

355   non-robust appearance of flow features. A robust FTLE ridge detection presents an opportunity to identify search regions and dispatch environmental clean-up resources.

The ensemble average is efficient at reducing the FTLE features in presumably unpredictable parts of the flow field, whereas some FTLE features remain very strong and articulated in the FTLE ensemble average. These are the features we expect to be good predictors of actual LCSs.

360   Distinct FTLE ridges remain visible in short time averages (Fig. 4). The time average effectively removes short-lived FTLE ridges over longer time period, but keeps them for short time averages (Fig. 9). LCSs could therefore be used for short term forecasting, e.g. three days, knowing that most small-scale and short-lived LCSs also persist at this forecasting length.

Process studies on particle transport

The continental shelf sea off LoVe is known to be a hot spot for fisheries due to its high nutrient concentrations, forming

365   feeding grounds and spawning banks for marine life (Sundby and Bratland, 1987; Sundby et al., 2013). The transport of relevant nutrients and material in this region is widely studied (e.g. Adlandsvik and Sundby, 1994; Röhrs et al., 2014). The LCS analysis presented here shed light on an additional mechanism for enabling cross-slope transport of nutrients that could play a role in sustaining biological production during summer, when nutrient levels in the photic layer are generally consumed following the spring bloom. As an example, important zooplankton sustaining fish stocks at LoVe, *Calanus Finmarchicus*,

370   overwinters at deeper depths off the continental shelf (Kaartvedt, 1996) and may be transported onto the continental shelf. The existence of persistent LCS transport barriers may hinder cross-slope transport during winter. Applying LCSs to different regions may reveal important transport barriers and material accumulation zones with high impact on local biology, and may be utilized to identify regions of high biological production (Johnsen et al., 2024).

5   Conclusions

375   LCS analysis provides a diagnostic tool for describing the particle transport in uncertain velocity fields. We show that the uncertainty of ocean model forecasts propagate into the FTLE fields. By employing time and ensemble averaging of ensemble FTLE fields, certain LCS detections may be separated from uncertain features. In particular, ensemble averaging retains flow structures at larger scales that are time-evolving, but predictable at specific times. These are often influenced by geomorphological constraint, or related to large scale circulation patterns. Large seasonal differences in LCSs due to changes in weather

380   and ocean conditions are observed. Because of flow field evolution, LCSs are shown to be more robust than persistent. LCS analysis adds value to operational forecasting only where these are robust, which can be judged by combining LCS analysis with ensemble prediction methods.

Code and data availability.   Archived data from the operational model runs of Barents-2.5 are disseminated on https://thredds.met.no/thredds/ fou-hi/barents_eps.html (Norwegian Meteorological Institute). Software for computing FTLE fields can be found on https://github.com/

385   mateuszmatu/LCS (Matuszak, 2024).

Author contributions.   FTLE analysis: MM. Seasonal analysis: MM, PEI. Circulation model: MI, JR. Manuscript preparation: MM, JR, MI, PEI. Study concept: JR.

Competing interests.   We declare absence of competing interests related to this work.

Acknowledgements. We acknowledge funding by the Research Council of Norway through grant nos. 237906 (CIRFA) and 300329 (EcoPulse).

References

Adlandsvik, B. and Sundby, S.: Modelling the transport of cod larvae from the Lofoten area, ICES Marine Science Symposia, 198, 379–392, 1994.

Allshouse, M. R., Ivey, G. N., Lowe, R. J., Jones, N. L., Beegle-Krause, C. J., Xu, J., and Peacock, T.: Impact of windage on ocean surface Lagrangian coherent structures, Environmental Fluid Mechanics, 17, 473–483, https://doi.org/10.1007/s10652-016-9499-3, 2017.

Badza, A., Mattner, T. W., and Balasuriya, S.: How sensitive are Lagrangian coherent structures to uncertainties in data?, Physica D: Nonlinear Phenomena, 444, 133 580, https://doi.org/10.1016/j.physd.2022.133580, 2023.

Beegle-Krause, C. J., Peacock, T., and Allshouse, M.: Exploiting Lagrangian coherent structures (LCS) for the calculation of oil spill and search-and-rescue drift patterns in the ocean, https://www.osti.gov/etdeweb/biblio/21547684, 2011.

Bøe, R., Bellec, V. K., Dolan, M. F. J., Buhl-Mortensen, P., Rise, L., and Buhl-Mortensen, L.: Cold-water coral reefs in the Hola glacial trough off Vesterålen, North Norway, Geological Society, London, Memoirs, 46, 309–310, https://doi.org/10.1144/M46.8, 2016.

Børve, E., Isachsen, P. E., and Nøst, O. A.: Rectified tidal transport in Lofoten–Vesterålen, northern Norway, Ocean Science, 17, 1753–1773, https://doi.org/10.5194/os-17-1753-2021, 2021.

Callies, J., Callies, J., Ferrari, R., Klymak, J. M., and Gula, J.: Seasonality in submesoscale turbulence, Nature communications, 6, 6862, https://doi.org/10.1038/ncomms7862, 2015.

Chen, G. and Han, G.: Contrasting Short-Lived With Long-Lived Mesoscale Eddies in the Global Ocean, Journal of Geophysical Research: Oceans, 124, 3149–3167, https://doi.org/10.1029/2019JC014983, 2019.

Christensen, K. H., Sperrevik, A. K., and Broström, G.: On the Variability in the Onset of the Norwegian Coastal Current, Journal of Physical Oceanography, 48, 723 – 738, https://doi.org/10.1175/JPO-D-17-0117.1, 2018.

Dagestad, K.-F. and Röhrs, J.: Prediction of ocean surface trajectories using satellite derived vs. modeled ocean currents, Remote Sensing of Environment, 223, 130–142, https://doi.org/10.1016/j.rse.2019.01.001, 2019.

Dagestad, K.-F., Röhrs, J., Breivik, O., and Ådlandsvik, B.: OpenDrift v1.0: a generic framework for trajectory modelling, Geoscientific Model Development, 11, 1405–1420, https://doi.org/10.5194/gmd-11-1405-2018, 2018.

de Aguiar, V., Röhrs, J., Johansson, A. M., and Eltoft, T.: Assessing ocean ensemble drift predictions by comparison with observed oil slicks, Frontiers in Marine Science, 10, https://doi.org/10.3389/fmars.2023.1122192, 2023.

Dong, H., Zhou, M., Hu, Z., Zhang, Z., Zhong, Y., Basedow, S. L., and Smith Jr., W. O.: Transport Barriers and the Retention of Calanus finmarchicus on the Lofoten Shelf in Early Spring, Journal of Geophysical Research: Oceans, 126, e2021JC017 408, https://doi.org/10.1029/2021JC017408, 2021.

Evensen, G.: Inverse methods and data assimilation in nonlinear ocean models, Physica D: Nonlinear Phenomena, 77, 108–129, https://doi.org/10.1016/0167-2789(94)90130-9, 1994.

Farazmand, M. and Haller, G.: Computing Lagrangian coherent structures from their variational theory, Chaos: An Interdisciplinary Journal of Nonlinear Science, 22, 013 128, https://doi.org/10.1063/1.3690153, 2012.

Furnes, G. and Sundby, S.: Upwelling and wind induced circulation in Vestfjorden, The Norwegian Coastal Current, Proceedings from the Norwegian Coastal Current Symposium, 1, 152–177, 1981.

Gascard, J.-C., Raisbeck, G., Sequeira, S., Yiou, F., and Mork, K. A.: The Norwegian Atlantic Current in the Lofoten basin inferred from hydrological and tracer data (129I) and its interaction with the Norwegian Coastal Current, Geophysical Research Letters, 31, https://doi.org/10.1029/2003GL018303, _eprint: https://agupubs.onlinelibrary.wiley.com/doi/pdf/10.1029/2003GL018303, 2004.

Gille, S., Metzger, J., and Tokmakian, R.: Seafloor Topography and Ocean Circulation, Oceanography, 17, 47–54, https://doi.org/10.5670/oceanog.2004.66, 2004.

Gouveia, M. B., Duran, R., Lorenzzetti, J. A., Assireu, A. T., Toste, R., Assad, L. P. d. F., and Gherardi, D. F. M.: Persistent meanders and
430   eddies lead to a quasi-steady Lagrangian transport pattern in a weak western boundary current, https://doi.org/10.48550/arXiv.2008.07620, 2020.

Haller, G.: Distinguished material surfaces and coherent structures in three-dimensional fluid flows, Physica D: Nonlinear Phenomena, 149, 248–277, https://doi.org/10.1016/S0167-2789(00)00199-8, 2001.

Haller, G.: Lagrangian Coherent Structures, Annual Review of Fluid Mechanics, 47, 137–162, https://doi.org/10.1146/annurev-fluid-010313-
435   141322, 2015.

Haller, G. and Yuan, G.: Lagrangian coherent structures and mixing in two-dimensional turbulence, Physica D: Nonlinear Phenomena, 147, 352–370, https://doi.org/10.1016/S0167-2789(00)00142-1, 2000.

Harrison, C. S. and Glatzmaier, G. A.: Lagrangian coherent structures in the California Current System – sensitivities and limitations, Geophysical & Astrophysical Fluid Dynamics, 106, 22–44, https://doi.org/10.1080/03091929.2010.532793, 2012.

440   Idžanović, M., Rikardsen, E. S. U., and Röhrs, J.: Forecast uncertainty and ensemble spread in surface currents from a regional ocean model, Frontiers in Marine Science, 10, https://doi.org/10.3389/fmars.2023.1177337, 2023.

Isachsen, P. E.: Baroclinic instability and the mesoscale eddy field around the Lofoten Basin, Journal of Geophysical Research: Oceans, 120, 2884–2903, https://doi.org/10.1002/2014JC010448, 2015.

Johnsen, I. A., Röhrs, J., and Kutti, T.: Exploring the role of food delivery mechanisms in regulating the distribution of the cold water coral
445   Lophelia pertusa, manuscript in preparation, 2024.

Kaartvedt, S.: Habitat preference during overwintering and timing of seasonal vertical migration of Calanus finmarchicus, Ophelia, 44, 145–156, https://doi.org/10.1080/00785326.1995.10429844, 1996.

Karrasch, D. and Haller, G.: Do Finite-Size Lyapunov Exponents detect coherent structures?, Chaos: An Interdisciplinary Journal of Nonlinear Science, 23, 043 126, https://doi.org/10.1063/1.4837075, 2013.

450   Koszalka, I., LaCasce, J. H., and Mauritzen, C.: In pursuit of anomalies—Analyzing the poleward transport of Atlantic Water with surface drifters, Deep Sea Research Part II: Topical Studies in Oceanography, 85, 96–108, https://doi.org/10.1016/j.dsr2.2012.07.035, 2013.

Lekien, F., Coulliette, C., Mariano, A. J., Ryan, E. H., Shay, L. K., Haller, G., and Marsden, J.: Pollution release tied to invariant manifolds: A case study for the coast of Florida, Physica D: Nonlinear Phenomena, 210, 1–20, https://doi.org/10.1016/j.physd.2005.06.023, 2005.

Leutbecher, M. and Palmer, T.: Ensemble forecasting, https://doi.org/10.21957/c0hq4yg78, 2007.

455   Lorenz, E. N.: Deterministic Nonperiodic Flow, Journal of Atmospheric Sciences, 20, 130 – 141, https://doi.org/10.1175/1520-0469(1963)020<0130:DNF>2.0.CO;2, 1963.

Matuszak, M.: mateuszmatu/LCS: FTLE computation software release for article, https://doi.org/10.5281/zenodo.10797134, 2024.

Mitchelson-Jacob, G. and Sundby, S.: Eddies of Vestfjorden, Norway, Continental Shelf Research, 21, 1901–1918, https://doi.org/10.1016/S0278-4343(01)00030-9, 2001.

460   Müller, M., Homleid, M., Ivarsson, K.-I., Køltzow, M. A. O., Lindskog, M., Midtbø, K. H., Andrae, U., Aspelien, T., Berggren, L., Bjørge, D., Dahlgren, P., Kristiansen, J., Randriamampianina, R., Ridal, M., and Vignes, O.: AROME-MetCoOp: A Nordic Convective-Scale Operational Weather Prediction Model, Weather and Forecasting, 32, 609–627, https://doi.org/10.1175/WAF-D-16-0099.1, 2017.

Norwegian Meteorological Institute: Barents-2.5 ocean and ice forecast model archive, [data set] last acess 2024-04-29, https://thredds.met.no/thredds/fou-hi/barents_eps.html.

465 Olascoaga, M. J. and Haller, G.: Forecasting sudden changes in environmental pollution patterns, Proceedings of the National Academy of Sciences, 109, 4738–4743, https://doi.org/10.1073/pnas.1118574109, 2012.

Peacock, T. and Haller, G.: Lagrangian coherent structures: The hidden skeleton of fluid flows, Physics Today, 66, 41–47, https://doi.org/10.1063/PT.3.1886, 2013.

Pierrehumbert, R. T. and Yang, H.: Global Chaotic Mixing on Isentropic Surfaces, Journal of the Atmospheric Sciences, 50, 2462–2480,
470   https://doi.org/10.1175/1520-0469(1993)050<2462:GCMOIS>2.0.CO;2, 1993.

Raj, R. P., Chafik, L., Nilsen, J. E. O., Eldevik, T., and Halo, I.: The Lofoten Vortex of the Nordic Seas, Deep Sea Research Part I: Oceanographic Research Papers, 96, 1–14, https://doi.org/10.1016/j.dsr.2014.10.011, 2015.

Ramos, A. G., García-Garrido, V. J., Mancho, A. M., Wiggins, S., Coca, J., Glenn, S., Schofield, O., Kohut, J., Aragon, D., Kerfoot, J., Haskins, T., Miles, T., Haldeman, C., Strandskov, N., Allsup, B., Jones, C., and Shapiro, J.: Lagrangian coherent structure assisted path planning
475   for transoceanic autonomous underwater vehicle missions, Scientific Reports, 8, 4575, https://doi.org/10.1038/s41598-018-23028-8, 2018.

Rosenstein, M. T., Collins, J. J., and De Luca, C. J.: A practical method for calculating largest Lyapunov exponents from small data sets, Physica D: Nonlinear Phenomena, 65, 117–134, https://doi.org/10.1016/0167-2789(93)90009-P, 1993.

Rossby, T., Ozhigin, V., Ivshin, V., and Bacon, S.: An isopycnal view of the Nordic Seas hydrography with focus on properties of the Lofoten Basin, Deep Sea Research Part I: Oceanographic Research Papers, 56, 1955–1971, https://doi.org/10.1016/j.dsr.2009.07.005, 2009.

480 Röhrs, J., Christensen, K. H., Vikebø, F., Sundby, S., Saetra, O., and Broström, G.: Wave-induced transport and vertical mixing of pelagic eggs and larvae, Limnology and Oceanography, 59, 1213–1227, https://doi.org/10.4319/lo.2014.59.4.1213, _eprint: https://onlinelibrary.wiley.com/doi/pdf/10.4319/lo.2014.59.4.1213, 2014.

Röhrs, J., Sutherland, G., Jeans, G., Bedington, M., Sperrevik, A. K., Dagestad, K.-F., Gusdal, Y., Mauritzen, C., Dale, A., and LaCasce, J. H.: Surface currents in operational oceanography: Key applications, mechanisms, and methods, Journal of Operational Oceanography,
485   0, 1–29, https://doi.org/10.1080/1755876X.2021.1903221, 2021.

Röhrs, J., Gusdal, Y., Rikardsen, E., Duran Moro, M., Brændshøi, J., Kristensen, N. M., Fritzner, S., Wang, K., Sperrevik, A. K., Idžanović, M., Lavergne, T., Debernard, J., and Christensen, K. H.: Barents-2.5km v2.0: An operational data-assimilative coupled ocean and sea ice ensemble prediction model for the Barents Sea and Svalbard, Geoscientific Model Development Discussions, pp. 1–31, https://doi.org/10.5194/gmd-2023-20, 2023.

490 Sakov, P., Counillon, F., Bertino, L., Lisæter, K. A., Oke, P. R., and Korablev, A.: TOPAZ4: an ocean-sea ice data assimilation system for the North Atlantic and Arctic, Ocean Science, 8, 633–656, https://doi.org/10.5194/os-8-633-2012, 2012.

Serra, M., Sathe, P., Rypina, I., Kirincich, A., Ross, S. D., Lermusiaux, P., Allen, A., Peacock, T., and Haller, G.: Search and rescue at sea aided by hidden flow structures, Nature Communications, 11, 2525, https://doi.org/10.1038/s41467-020-16281-x, 2020.

Shadden, S. C., Lekien, F., and Marsden, J. E.: Definition and properties of Lagrangian coherent structures from finite-time Lyapunov expo-
495   nents in two-dimensional aperiodic flows, Physica D: Nonlinear Phenomena, 212, 271–304, https://doi.org/10.1016/j.physd.2005.10.007, 2005.

Shchepetkin, A. F. and McWilliams, J. C.: The regional oceanic modeling system (ROMS): a split-explicit, free-surface, topography-following-coordinate oceanic model, Ocean Modelling, 9, 347–404, https://doi.org/10.1016/j.ocemod.2004.08.002, 2005.

Sperrevik, A. K., Röhrs, J., and Christensen, K. H.: Impact of data assimilation on Eulerian versus Lagrangian estimates of upper ocean
500   transport, Journal of Geophysical Research: Oceans, 122, 5445–5457, https://doi.org/10.1002/2016JC012640, 2017.

Sundby, S.: Influence of bottom topography on the circulation at the continental shelf off northern Norway, Fiskeridirektoratets Skrifter Serie Havundersokelser, 17, 501–519, 1984.

Sundby, S. and Bratland, P.: Spatial distribution and production of eggs from Northeast-arctic cod at the coast of Northern Norway 1983–1985, Fisken og havet, 1, 1987.

505 Sundby, S., Fossum, P., Sandvik, A. D., Vikebø, F., Aglen, A., Buhl-Mortensen, L., Folkvord, A., Bakkeplass, K., Buhl-Mortensen, P., Johannessen, M., Jørgensen, M. S., Kristiansen, T., Landra, C. S., Myksvoll, M. S., and Nash, R. D. M.: KunnskapsInnhenting Barentshavet–Lofoten–Vesterålen (KILO), 188 s., https://imr.brage.unit.no/imr-xmlui/handle/11250/113923, publisher: Havforskningsinstituttet, last access: 17 April 2024, 2013.

Søiland, H. and Rossby, T.: On the structure of the Lofoten Basin Eddy, Journal of Geophysical Research: Oceans, 118, 4201–4212,
510 https://doi.org/https://doi.org/10.1002/jgrc.20301, 2013.

Trodahl, M. and Isachsen, P. E.: Topographic Influence on Baroclinic Instability and the Mesoscale Eddy Field in the Northern North Atlantic Ocean and the Nordic Seas, Journal of Physical Oceanography, 48, 2593–2607, https://doi.org/10.1175/JPO-D-17-0220.1, 2018.

Truesdell, C. and Noll, W.: The Non-Linear Field Theories of Mechanics, in: The Non-Linear Field Theories of Mechanics, edited by Truesdell, C., Noll, W., and Antman, S. S., pp. 57–73, Springer, Berlin, Heidelberg, https://doi.org/10.1007/978-3-662-10388-3_1, 2004.

515 van Sebille, E., Griffies, S. M., Abernathey, R., Adams, T. P., Berloff, P., Biastoch, A., Blanke, B., Chassignet, E. P., Cheng, Y., Cotter, C. J., Deleersnijder, E., Döös, K., Drake, H. F., Drijfhout, S., Gary, S. F., Heemink, A. W., Kjellsson, J., Koszalka, I. M., Lange, M., Lique, C., MacGilchrist, G. A., Marsh, R., Mayorga Adame, C. G., McAdam, R., Nencioli, F., Paris, C. B., Piggott, M. D., Polton, J. A., Rühs, S., Shah, S. H. A. M., Thomas, M. D., Wang, J., Wolfram, P. J., Zanna, L., and Zika, J. D.: Lagrangian ocean analysis: Fundamentals and practices, Ocean Modelling, 121, 49–75, https://doi.org/10.1016/j.ocemod.2017.11.008, 2018.

520 Zimmerman, J.: The tidal whirlpool: A review of horizontal dispersion by tidal and residual currents, Netherlands Journal of Sea Research, 20, 133–154, https://doi.org/10.1016/0077-7579(86)90037-2, 1986.